Estimating Eddy Stresses by Fitting Dynamics to Observations Using a Residual-Mean Ocean Circulation Model and Its Adjoint

David Ferreira, John Marshall, and Patrick Heimbach

Department of Earth, Atmospheric, and Planetary Sciences, Massachusetts Institute of Technology, Cambridge, Massachusetts

(Manuscript received 8 June 2004, in final form 11 March 2005)

ABSTRACT

A global ocean circulation model is formulated in terms of the "residual mean" and used to study eddy–mean flow interaction. Adjoint techniques are used to compute the three-dimensional eddy stress field that minimizes the departure of the coarse-resolution model from climatological observations of temperature. The resulting 3D maps of eddy stress and residual-mean circulation yield a wealth of information about the role of eddies in large-scale ocean circulation. In eddy-rich regions such as the Southern Ocean, the Kuroshio, and the Gulf Stream, eddy stresses have an amplitude comparable to the wind stress, of order 0.2 N m^{-2}, and carry momentum from the surface down to the bottom, where they are balanced by mountain form drag. From the optimized eddy stress, 3D maps of horizontal eddy diffusivity κ are inferred. The diffusivities have a well-defined large-scale structure whose prominent features are 1) large values of κ (up to 4000 m^2 s^{-1}) in the western boundary currents and on the equatorial flank of the Antarctic Circumpolar Current and 2) a surface intensification of κ, suggestive of a dependence on the stratification N^2. It is shown that implementation of an eddy parameterization scheme in which the eddy diffusivity has an N^2 dependence significantly improves the climatology of the ocean model state relative to that obtained using a spatially uniform diffusivity.

1. Introduction

The parameterization of the transfer properties of geostrophic eddies remains a primary challenge and demand of large-scale ocean circulation models used for climate research. The eddy scale contains most of the kinetic energy of the global ocean circulation and yet is not resolved by coarse-grained models and must be treated as a subgrid-scale process. The conventional approach is to phrase the problem in terms of an eddy diffusivity that relates the eddy flux of a (quasi-conserved) quantity to its large-scale gradient. However, the spatial distribution of the diffusivity and even its sign are uncertain. Here, a new approach to the problem is pursued: a novel formulation of the governing equations is employed along with a sophisticated inverse technique to estimate the subgrid-scale fluxes that bring the model into consistency with observations.

The model is formulated in terms of the meteorologist's "residual mean" (Andrews and McIntyre 1976), appropriately modified for application to ocean circulation as described in section 2. Eddy terms appear primarily as a forcing of the residual-mean momentum equation—a vertical divergence of an eddy stress that can be interpreted as a vertical eddy form drag. Rather than attempt to parameterize the eddy stresses, in section 4 we infer their large-scale pattern by using them as control parameters in an optimization calculation. The associated residual momentum balance and meridional overturning circulation is discussed in section 5. In section 6, we interpret our results from the more conventional perspective of "eddy diffusivities," κ. We find that the κ implied by our eddy stress maps are not constant but show strong horizontal and vertical spatial variations. In particular, they are surface intensified (reaching values of several thousand meters squared per second) and decay to near-zero value at depth, suggestive of a dependence on the stratification N^2. Incorporation of an N^2-dependent eddy diffusivity in the

---

Corresponding author address: Dr. David Ferreira, Department of Earth, Atmospheric, and Planetary Sciences, Massachusetts Institute of Technology, Room 54-1515, 77 Massachusetts Avenue, Cambridge, MA 02139.
E-mail: dfer@mit.edu

Gent and McWilliams (1990, hereinafter GM) eddy parameterization scheme leads to improvements in model performance. We conclude in section 7.

2. Residual-mean framework

It is a great conceptual as well as computational advantage to phrase the eddy–mean flow interaction problem in terms of residual-mean theory. In that framework, tracers are advected by residual-mean velocities obtained by stepping forward a residual-mean momentum equation in which eddy stresses appear as forcing terms. These eddy stresses can then become the focus of a least squares calculation in which they are adjusted to "fit" the model to observations. Adjustment of the eddy stress terms results, of necessity, in an adiabatic rearrangement of the fluid maintaining tracer properties. We begin, then, by reviewing key elements of residual-mean theory.

a. The residual-mean buoyancy equation

The formulation of the residual-mean buoyancy equation and the definition of the eddy-induced velocity used here follow from Andrews and McIntyre (1976) and Treguier et al. (1997). Recently, more sophisticated formulations have been proposed in an attempt to better separate diabatic and adiabatic eddy buoyancy flux components or improve the treatment of boundary conditions (see Held and Schneider 1999; Marshall and Radko 2003; Ferrari and Plumb 2003; Canuto and Dubovikov 2005; among others). However, the formulation of Treguier et al. (1997) captures the essential physics and is preferred in the present discussion.

Assuming a separation between a mean (denoted by an overbar) and an eddy (denoted by a prime) fields, the mean buoyancy budget is given by

$$\frac{\partial \overline{b}}{\partial t} + \overline{\mathbf{v}} \cdot \nabla \overline{b} = -\nabla \cdot \overline{\mathbf{v}'b'} + \mathcal{S}, \tag{1}$$

where $\mathcal{S}$ are buoyancy sources (surface forcings and vertical diffusivity). Since eddy buoyancy fluxes tend to be skewed (directed along $\overline{b}$ surfaces) in the ocean interior, a nondivergent eddy-induced velocity, $\mathbf{v}^*$, can be introduced to capture their effects. The eddy-induced velocity can be written in terms of a (vector) streamfunction $\boldsymbol{\Psi}^*$:

$$\mathbf{v}^* = -\nabla \times \boldsymbol{\Psi}^*, \tag{2}$$

where

$$\boldsymbol{\Psi}^* = \left(\frac{\overline{v'b'}}{\overline{b}_z}, -\frac{\overline{u'b'}}{\overline{b}_z}, 0 \right). \tag{3}$$

Defining the residual velocities and the residual eddy flux as

$$\mathbf{v}_{\mathrm{res}} = \overline{\mathbf{v}} + \mathbf{v}^* \quad \text{and} \tag{4}$$

$$\mathbf{F}_{\mathrm{res}} = \frac{\overline{\mathbf{v}'b'} \cdot \nabla \overline{b}}{\overline{b}_z} \hat{\mathbf{z}}, \tag{5}$$

the mean buoyancy Eq. (1) becomes

$$\frac{\partial \overline{b}}{\partial t} + \mathbf{v}_{\mathrm{res}} \cdot \nabla \overline{b} = -\nabla \cdot \mathbf{F}_{\mathrm{res}} + \mathcal{S}. \tag{6}$$

Complications arise near horizontal boundaries: $\mathbf{v}_{\mathrm{res}} \cdot \hat{\mathbf{n}}$ and $\mathbf{F}_{\mathrm{res}} \cdot \hat{\mathbf{n}}$ (where $\hat{\mathbf{n}}$ is a unit normal to the boundary) are not necessarily zero even though $\overline{\mathbf{v}'b'} \cdot \hat{\mathbf{n}} = 0$. Following Treguier et al. (1997), the domain is divided into an adiabatic interior where the eddy flux is "skew" ($\mathbf{F}_{\mathrm{res}} \simeq 0$) and a surface layer of thickness h_s where eddy fluxes develop a diabatic component as they become parallel to the boundary and isopycnal slopes steepen under the influence of turbulent mixing and air–sea exchanges. This surface layer encompasses the mixed layer but also includes a transition layer connecting the base of the mixed layer to the low-mixing region of the ocean interior (see Ferrari and McWilliams 2005, manuscript submitted to *Ocean Modell.*). In this surface layer, the definition of $\boldsymbol{\Psi}^*$ is modified by assuming that the return flow is spread within the layer:[1]

$$\boldsymbol{\Psi}^* = \left(\frac{\overline{v'b'}}{\overline{b}_z}, -\frac{\overline{u'b'}}{\overline{b}_z}, 0 \right)\Bigg|_{z=-h_s} \mu, \quad -h_s < z < 0, \tag{7}$$

where μ is a function that changes from 0 at the surface to 1 at $z = h_s$. Note that μ and h_s can be functions of x, y, and t. A similar diabatic layer can be defined at the bottom of the ocean. Therefore, $\mathbf{v}_{\mathrm{res}}$ and $\mathbf{F}_{\mathrm{res}}$ remain unchanged in the interior, but they satisfy a non-normal-flux condition at the top and bottom; more precisely, $\boldsymbol{\Psi}^* = 0$ at all boundaries.

Equation (6) underscores that in a turbulent ocean it is $\mathbf{v}_{\mathrm{res}}$ and not $\overline{\mathbf{v}}$ that advects $\overline{b}$. At equilibrium, advection by the residual circulation balances the diabatic terms. Away from the surface, the diabatic sources $\mathcal{S}$ and the eddy diapycnal component $\mathbf{F}_{\mathrm{res}}$ decrease, and so $\mathbf{v}_{\mathrm{res}}$ tends to be along $\overline{b}$ surfaces ($\mathbf{v}_{\mathrm{res}} \cdot \nabla \overline{b} \simeq 0$; see Kuo et al. 2005 for an example). Using the quasi-adiabaticity of mesoscale eddies in the ocean interior, we simplify the buoyancy Eq. (6) by neglecting the diabatic eddy flux component $\mathbf{F}_{\mathrm{res}}$ although it may be im-

---

[1] Accordingly, the residual flux $\mathbf{F}_{\mathrm{res}}$ is also modified. It is obtained directly using its definition as $\overline{\mathbf{v}'b'}$ minus the skew flux: $\mathbf{F}_{\mathrm{res}} = \overline{\mathbf{v}'b'} + \boldsymbol{\Psi}^* \times \nabla \overline{b}$.

portant near the surface (see Marshall and Radko 2003; Kuo et al. 2005):

$$\frac{\partial \overline{b}}{\partial t} + \mathbf{v}_{\text{res}} \cdot \boldsymbol{\nabla} \overline{b} = \mathcal{S}. \tag{8}$$

b. The residual momentum equation

Along with the residual-mean buoyancy equation, we must formulate the residual-mean momentum equation. It is useful to first consider the momentum equation in the planetary geostrophic limit, in which advection of momentum is neglected entirely:

$$f\hat{\mathbf{z}} \times \overline{\mathbf{v}} = -\frac{1}{\rho_o}\boldsymbol{\nabla} p + \frac{1}{\rho_o}\frac{\partial \tau^w}{\partial z}.$$

Then, since $\overline{\mathbf{v}} = \mathbf{v}_{\text{res}} + \boldsymbol{\nabla} \times \boldsymbol{\Psi}^*$ from Eq. (4), the above may be written as follows:

$$f\hat{\mathbf{z}} \times \mathbf{v}_{\text{res}} = -\frac{1}{\rho_o}\boldsymbol{\nabla} p + \frac{1}{\rho_o}\frac{\partial(\tau^w + \tau^e)}{\partial z}, \tag{9}$$

where, using Eq. (2), we identify

$$\tau^e = (\tau^e_x, \tau^e_y) = \rho_o f \boldsymbol{\Psi}^* \tag{10}$$

as an eddy stress that vanishes ($\boldsymbol{\Psi}^* = 0$) at the top and bottom of the ocean (see section 2c for a physical interpretation).

If the advection of momentum is not neglected, we may write the time-mean momentum budget thus:

$$\frac{\partial \overline{\mathbf{v}}}{\partial t} + \overline{\mathbf{v}} \cdot \boldsymbol{\nabla}\overline{\mathbf{v}} + f\hat{\mathbf{z}} \times \overline{\mathbf{v}} = -\frac{1}{\rho_o}\boldsymbol{\nabla} p + \frac{1}{\rho_o}\frac{\partial \tau^w}{\partial z} - \overline{\mathbf{v}' \cdot \boldsymbol{\nabla}\mathbf{v}'}, \tag{11}$$

where the last terms on the rhs are Reynolds stresses due to eddies. Since the residual velocity has the same magnitude as the Eulerian velocity[2] and the advection terms in Eq. (11) are of order Rossby number R_o relative to the Coriolis terms, we may replace $\overline{\mathbf{v}}$ in the advection terms by $\mathbf{v}_{\text{res}}$, to leading order in R_o:

$$\frac{\partial \mathbf{v}_{\text{res}}}{\partial t} + \mathbf{v}_{\text{res}} \cdot \boldsymbol{\nabla}\mathbf{v}_{\text{res}} + f\hat{\mathbf{z}} \times \mathbf{v}_{\text{res}} \simeq -\frac{1}{\rho_0}\boldsymbol{\nabla}_p + \frac{1}{\rho_0}\frac{\partial(\tau^w + \tau^e)}{\partial z} - \overline{\mathbf{v}' \cdot \boldsymbol{\nabla}\mathbf{v}'}, \tag{12}$$

where τ^e is given by Eq. (10). Equation (12) retains the primitive equation form because we have kept some, but not all, of the $O(R_o)$ terms. This is not an issue as long as the $O(R_o)$ terms are negligible, which is the case in coarse-resolution ocean models such as the one used here (see description in section 3a). However, this does not hold in general, and Eq. (12) must only be used in appropriate circumstances.

A zonal-average form of Eq. (12) was made use of in Wardle and Marshall (2000) where the eddy terms on the rhs were approximated by their quasigeostrophic form and related to eddy quasigeostrophic potential vorticity (PV) fluxes. Plumb and Ferrari (2005) discuss the zonal-average form of Eq. (12) in some detail, relaxing quasigeostrophic approximations. Likewise, here we do not assume quasigeostrophic scaling and work with the following residual momentum balance appropriate to the large scale:

$$\frac{\partial \mathbf{v}_{\text{res}}}{\partial t} + \mathbf{v}_{\text{res}} \cdot \boldsymbol{\nabla}\mathbf{v}_{\text{res}} + f\hat{\mathbf{z}} \times \mathbf{v}_{\text{res}} = -\frac{1}{\rho_0}\boldsymbol{\nabla}_p + \frac{1}{\rho_0}\frac{\partial(\tau^w + \tau^e)}{\partial z} + \nu\nabla^2\mathbf{v}_{\text{res}}. \tag{13}$$

Equation (13) has the same form as the "primitive equations" albeit with a reinterpretation of the terms (residual, rather than Eulerian mean velocities), and the forcing term on the rhs has an eddy contribution that has exactly the same status as the wind stress, except that it exists in the interior of the fluid and vanishes at the boundaries. Note that the Reynolds stress terms are parameterized by a viscosity ν acting, in this case, on the residual flow. This is typically done in large-scale ocean models but has little physical justification (see the discussion in Marshall 1981).

We call the key equations of our model—Eqs. (8), (10), and (13)—the Transformed Eulerian Mean (TEM) model.

c. Physical interpretation of eddy stresses

In the interior of the ocean, the eddy stress [Eq. (3)] has clear connections with the following:

1) the vertical component of the Eliassen–Palm flux (see Andrews et al. 1987),
2) the stretching component of an eddy PV flux (e.g., Marshall 1981), and
3) the eddy form stress or the vertical flux of momentum resulting from the correlation between eddy pressure fluctuations p' and isopycnal displacements η' since $\rho_0 f(\overline{v'b'}/\overline{b}_z) \sim \rho_0 f\overline{v'\eta'} \sim \overline{p'_x\eta'}$ using geo-

---

[2] To see this, suppose that $b' \sim \overline{b}_z\eta'$, where η' is the isopycnal displacement; we find that $(\partial/\partial z)(\overline{\mathbf{v}'b'}/\overline{b}_z) \sim (r\eta'\overline{v}/H)$, where r is the ratio of the eddy to the mean velocity $(v'/\overline{v})$ and H is the vertical scale of mesoscale eddies. Thus $\mathbf{v}_{\text{res}} = \overline{\mathbf{v}}[1 + O(r\eta'/H)]$. Taking $H \sim 1000$ m and $\eta' \sim 100$ m, $(r\eta'/H)$ remains less than unity since r ranges typically from 1 in jets to 10 in the interior of gyres.

strophic balance (see Rhines 1979). For example, a positive zonal eddy stress corresponds to a downward flux of eastward momentum.

3. Solving for the eddy stresses

The assumption underlying our study is that the largest uncertainty in the TEM equations is not the form of $\mathcal{S}$ in Eq. (8) (although, to be sure, mixing processes are uncertain too) but rather the form of the eddy stresses, τ^e in Eq. (13). Rather than attempt to close for the eddy terms through use of an eddy diffusivity, we first attempt to construct them by fitting a TEM ocean model to observations using an "adjoint technique" and a least squares method developed in the Estimating the Circulation and Climate of the Ocean (ECCO) project (Stammer et al. 2002).

a. *The forward model and its adjoint*

The TEM equations are solved numerically using the Massachusetts Institute of Technology (MIT) general circulation model (Marshall et al. 1997a,b) and its adjoint. The latter is generated automatically using the transformation of algorithms in FORTRAN (TAF) software (Giering and Kaminski 1998), as described in Marotzke et al. (1999). The model has a horizontal resolution of 4° and 15 levels in the vertical. The geometry is "realistic" except for the absence of the Arctic Ocean; bathymetry is represented by partial cells (Adcroft et al. 1997). The model is forced by observed monthly mean climatological surface wind stresses (Trenberth et al. 1990) and heat fluxes [National Centers for Environmental Prediction–National Center for Atmospheric Research (NCEP–NCAR) reanalysis (Kalnay et al. 1996)]. Sea surface temperature and salinity are restored toward observed monthly mean climatological values (Levitus and Boyer 1994; Levitus et al. 1994) with time scales of 2 and 6 months, respectively. However, no representation of sea ice is included. The vertical viscosity and diffusion are 10^{-3} $\mathrm{m^2\,s^{-1}}$ and $3 \times 10^{-5}\ \mathrm{m^2\,s^{-1}}$ respectively, while horizontal viscosity is set to $5 \times 10^5\ \mathrm{m^2\,s^{-1}}$ to resolve the Munk boundary layer. Convection is parameterized by enhanced vertical diffusion whenever the water column becomes statically unstable. In reference solutions of the model, the effect of mesoscale eddies on tracers is parameterized by the eddy-induced transport of GM and an isopycnal mixing (Redi 1982). Tapering of the isopycnal slopes is done adiabatically using the scheme of Danabasoglu and McWilliams (1995). During the optimization, the GM scheme is not used since temperature and salinity are advected by the residual velocity driven by winds and eddy stresses. However, the isopycnal mixing tensor $\mathcal{R}$ is retained with a coefficient of 1000 $\mathrm{m^2\,s^{-1}}$:

$$\frac{\partial \overline{T}}{\partial t} + \mathbf{v}_{\mathrm{res}} \cdot \nabla \overline{T} = \mathcal{S}_T + \mathcal{R}(\overline{T}) \quad \text{and} \tag{14}$$

$$\frac{\partial \overline{S}}{\partial t} + \mathbf{v}_{\mathrm{res}} \cdot \nabla \overline{S} = \mathcal{S}_S + \mathcal{R}(\overline{S}), \tag{15}$$

where $\mathcal{S}_T$ and $\mathcal{S}_S$ are the sources and sinks of potential temperature and salinity, respectively. Thus, in the adiabatic limit, $\mathbf{v}_{\mathrm{res}}$ advects all tracers.

b. *Least squares method*

The control variables are the two components of the eddy streamfunction $\mathbf{\Psi}^* = (\mathbf{\Psi}_x^*, \mathbf{\Psi}_y^*)$ [see Eq. (10)]. We focus here on the climatological form of the eddy stresses and assume that they depend only on space. The eddy stresses are inferred by an iterative method. The TEM equations are solved numerically, and the quality of the solution is determined by a cost function J, a measure of the departure of the model from observations. The cost function also places (reasonable) constraints on the eddy stresses. The adjoint model then provides the sensitivities $\partial J/\partial \tau_x^e$ and $\partial J/\partial \tau_y^e$ of J relative to each component of the 3D fields, τ_x^e and τ_y^e. Using a line-searching algorithm (Gilbert and Lemaréchal 1989), the eddy stresses are adjusted in the sense to reduce J—the procedure is repeated until convergence.

Each iteration is 100 yr in length—100 yr forward and 100 backward. Starting from a state of rest, the initial conditions for potential temperature and salinity are taken from the Levitus climatology (Levitus and Boyer 1994; Levitus et al. 1994). In a first experiment, E1, one component of the cost function, which we call J_1, measures the misfit between the 100-yr mean modeled temperature and climatological observations. The misfit is weighted by an a priori error based on the observed temperature (Levitus and Boyer 1994). In addition, equatorial points, where a coarse-resolution model is expected to do a poor job, are down-weighted. An additional penalty, J_2, ensures that the eddy stresses remain within physical bounds. Observations suggest (see Johnson and Bryden 1989) that the eddy stress can balance the surface wind stress and hence reaches magnitudes of a few tenths of newtons per meter squared. Thus J_2 is built so that the eddy stress can vary in an unconstrained manner between $\pm 0.4\ \mathrm{N\,m^{-2}}$ (somewhat larger than the magnitude of the applied wind stress), but variations outside these limits are heavily penalized. Details can be found in the appendix.

A "first guess" to the eddy stress is computed from

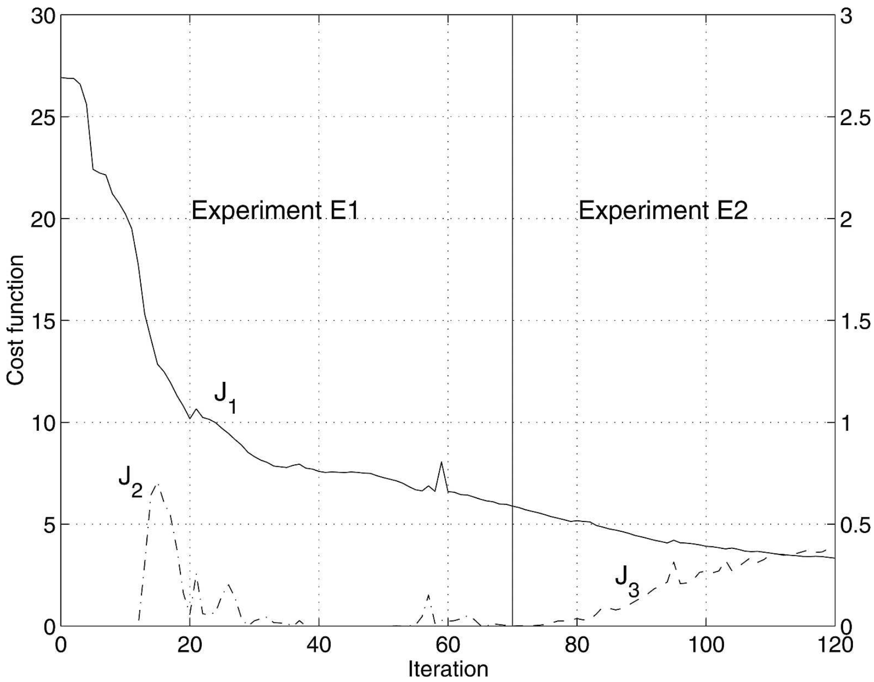

FIG. 1. Cost function: temperature component J_1 (solid), eddy stress component J_2 (dashed–dotted), and wind stress component J_3 (dashed) as a function of the number of iteration. Iterations 0–70 correspond to the experiment E1, and iterations 70–120 correspond to experiment E2. Note the different scales for (left) J_1 and J_2 and (right) J_3. Note also that J_3 is only defined in E2.

Eq. (3), assuming that the eddy buoyancy flux is directed downgradient:

$$\tau^e = \rho_0 f \kappa (s_{\rho y}, -s_{\rho x}), \tag{16}$$

where $s_{\rho x}$ and $s_{\rho y}$ are the isopycnal slopes in the zonal and meridional direction and κ is a uniform eddy diffusivity equal to 1000 $\mathrm{m}^2\,\mathrm{s}^{-1}$. The slopes were diagnosed from a 100-yr run whose setup is identical to that used in the optimization, but using the GM eddy parameterization instead of the TEM formulation. This run and the first sweep of the iterative procedure are almost identical, although the isopycnal slope is computed interactively in the former, while it is prescribed in the latter. This similarity is to be expected since, in the planetary geostrophic limit, the GM parameterization is equivalent to the TEM formulation with an eddy stress evaluated as in Eq. (16) (Gent et al. 1995; Greatbatch 1998; Wardle and Marshall 2000). This choice of a first-guess eddy stress provides a useful reference for comparison with the optimized stress.

To test the robustness of our results, a second experiment (E2) is conducted in which the climatological zonal and meridional wind stresses τ_x^w and τ_y^w are also included as control variables. To constrain them, a third component to the cost function is constructed, J_3, which penalizes the drift of the surface wind stress from climatological observations weighted by a priori errors. The latter were obtained from the ECCO project (Stammer et al. 2002) and were computed as the rms difference between National Aeronautics and Space Administration (NASA) scatterometer observations and the European Centre for Medium-Range Forecasts reanalysis. The optimized eddy stress from the first experiment E1 is taken as the first guess of E2.

4. Optimized solutions

In experiment E1, the cost function J_1 decreases by 80% after 70 iterations, from 26.9 down to 5.9 (Fig. 1)—the target value of about 1 implies that the model is, on average, within observational uncertainties. The J_2 component of the cost function, constraining the magnitude of the eddy stresses, increases from 0, reaches a maximum (0.7) around iteration 15, and then decreases to remain almost null. The first iteration of experiment E2 reproduces the last iteration of experiment E1. Over the 50 iterations of E2, the J1 component decreases further to 3.5 whilst the J_2 component remains around zero. Over the course of the 120 iterations, the temperature cost function J_1 decreases by

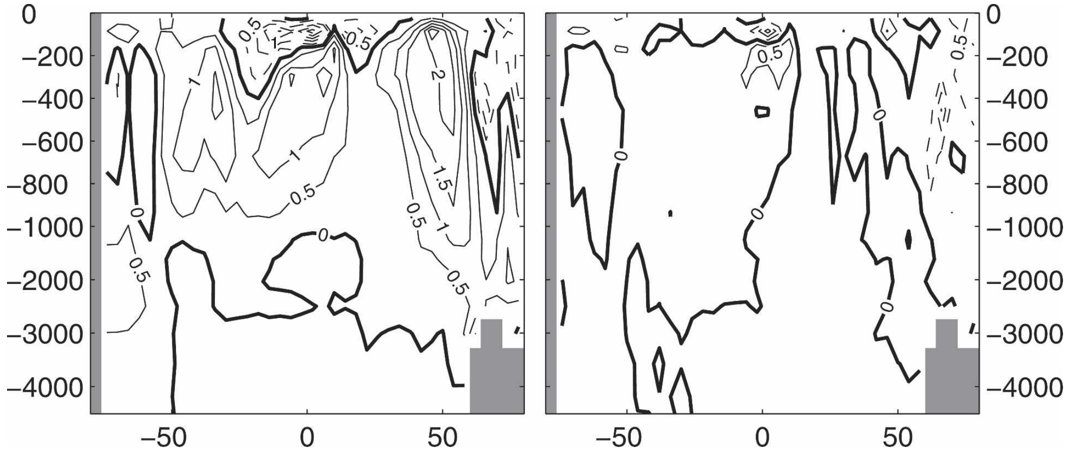

FIG. 2. Zonal mean departure of the 100-yr mean model temperature from climatological mean observations (left) before (first iteration of E1) and (right) after (last iteration of E2) optimization. The positive and negative contours are solid and dashed, respectively. The zero contour is highlighted, and the contour interval 0.5 K.

about one order of magnitude. The wind cost function J_3 starts from 0 and slowly increases up to 0.4 as the climatological mean wind stress is modified.

The results of experiments E1 and E2 are indeed very similar, experiment E2 only resulting in small adjustments to the eddy stress mainly near the surface. Therefore, we only discuss the solution at the first iteration of E1 and last iteration of E2, corresponding respectively to the first guess and "optimized" eddy stresses. Figure 2 displays the zonal mean difference between the time-mean modeled and observed temperatures for these two iterations. At the first iteration, the model thermocline is too warm with a drift reaching 2.5 K at 40°N; the model's Antarctic Intermediate Water is too warm by 1.5 K. The other prominent feature is that surface waters in the Tropics are too cool by 3 K. Deep waters are too cold, but the errors there are small as a result of the relatively short spinup. As noted above, this pattern of error is almost exactly similar to the one obtained from a run employing the GM parameterization with a uniform eddy diffusivity because of our choice of the first guess eddy stress. After optimization, the drift is significantly reduced everywhere except very close to the equator. This is perhaps to be expected given the down-weighting of the equatorial regions in the cost function J_1. The model's Antarctic Mode Water remains too warm, but the drift is reduced to only 0.5 K. In the Northern Hemisphere, the maximum drift of the model relative to observations is reduced to 1 K. Note that the improvement of the temperature field is not at the expense of the salinity field. The latter, albeit not entering the cost function, is actually slightly improved. An offline computation of a salinity cost function similar to that for temperature shows a decrease of about 20% between the first iteration of experiment E1 and the last of E2.

Eddy stress and wind stress

The first guess and optimized zonal eddy stress are shown at three different depths in Figs. 3–5. The eddy stress at the first iteration is relatively small as compared with the wind with a maximum of 0.06 N m^{-2} in the Antarctic Circumpolar Current (ACC). It is mainly positive (i.e., directed eastward) except for a negative zonal band at the equator and at the northern and southern boundaries. The main feature is a positive pattern extending zonally in the Southern Ocean with a maximum in the Indian sector. There are secondary maxima (of 0.01 N m^{-2}) at the western boundaries around 40°N in the Pacific and Atlantic and in the Labrador and Norwegian Seas. The large-scale pattern reflects the spatial distribution of the isopycnal slope.

The optimized eddy stress has a much larger amplitude with peak values reaching 0.2 N m^{-2} in the North Atlantic and in the ACC. Although the positive zonal band in the Southern Ocean remains the prominent feature, one can observe significant signals in the Northern Hemisphere. A zonal strip of positive eddy stress extends across the Pacific and Atlantic basins at 40°N. The signal is particularly strong and intensified on the western margin in the latter. However, at 170 m, the eddy stress is somewhat larger in the Pacific than in the Atlantic and intensifies on the western margins in both basins (not shown). One observes a maximum of negative eddy stress south of Greenland (up to 0.2 N m^{-2}). Note that the optimized stresses in regions of intense convection should be taken with caution since

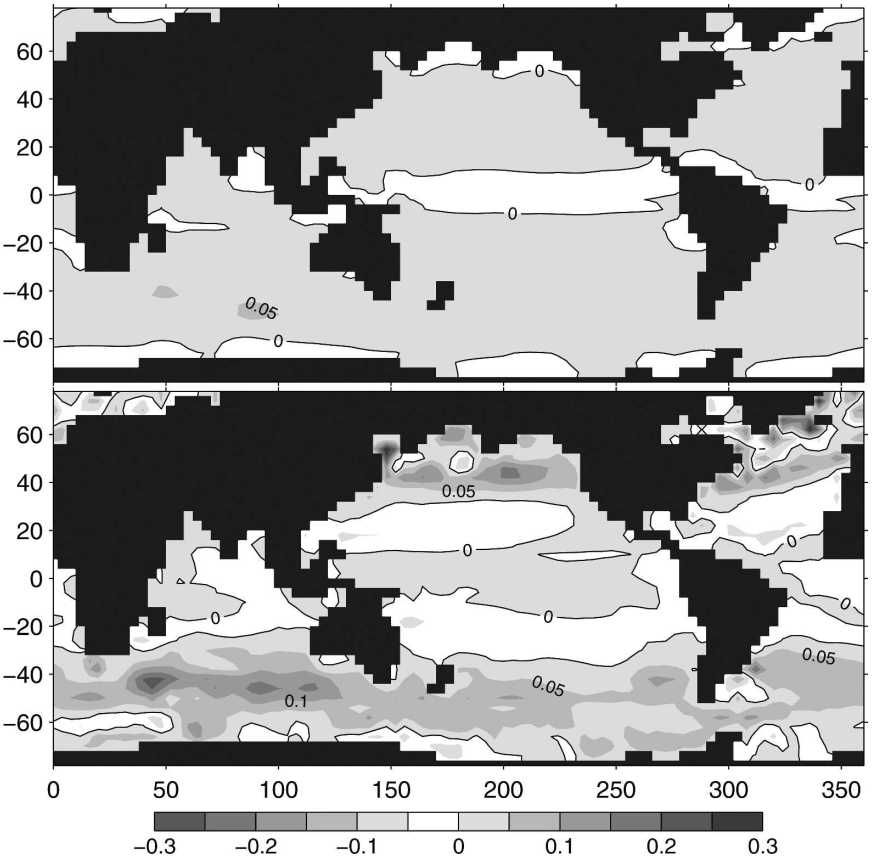

FIG. 3. Zonal eddy stress (N m^{-2}) at 50-m depth (top) before (first guess) and (bottom) after optimization (last iteration of E2). The contour interval is 0.05 N m^{-2}, and the zero contour is highlighted.

the model only uses a very simple convection parameterization (as described in Marshall and Schott 1999). In addition, the absence of outflow from the Arctic Ocean probably has a deleterious effect near the northern boundary. Nevertheless, the eddy stress near the surface exhibits an overall increase in strength in the North Pacific and Atlantic, as well as in the ACC, and has a magnitude comparable to the applied surface wind stress.

Interestingly, the optimized eddy stress in the Tropics (20°S–20°N) remains relatively small ($\leq$0.05 N m^{-2}), but its sign has been reversed. The eddy stress is positive near the equator and is surrounded by two negative bands centered at ±20°. This is particularly striking in the Pacific Ocean. The sign reversal extends vertically through the water column down to 3000 m.

Changes in subsurface stresses are as dramatic as those at the surface, as can be seen at a depth of 360 m (Fig. 4). The initial eddy stress is dominated by a large-scale positive pattern of ~0.15 N m^{-2} in the Southern Ocean. The optimized eddy stress along the path of the ACC is increased by 25% relative to the initial stress. The signal is spread latitudinally and is slightly shifted northward, particularly in the vicinity of the Kerguelen Plateau. In the northern Pacific Ocean, a patch of large positive eddy stress has appeared near the western boundary at 40°N (an increase from 0.04 to 0.15 N m^{-2}) while, in the North Atlantic, the first-guess positive eddy stress in the subpolar gyre is slightly intensified. In the Tropics, the eddy stress has changed signs during the optimization to become negative near the equator and positive around 20°S and 20°N.

Moving down the water column to a depth of 1810 m (Fig. 5), the initial eddy stress shows no significant signal outside the Southern Ocean. In the region of the ACC, a large (0.15 N m^{-2}) positive eddy stress remains in evidence. Elsewhere, the eddy stress magnitude does not exceed 0.05 N m^{-2} except for a small negative patch in the Labrador Sea reflecting the large isopycnal slopes induced by deep convection. The optimized eddy stress has a similar pattern, although it is somewhat less zonally symmetric in the ACC. In the Tropics, the op-

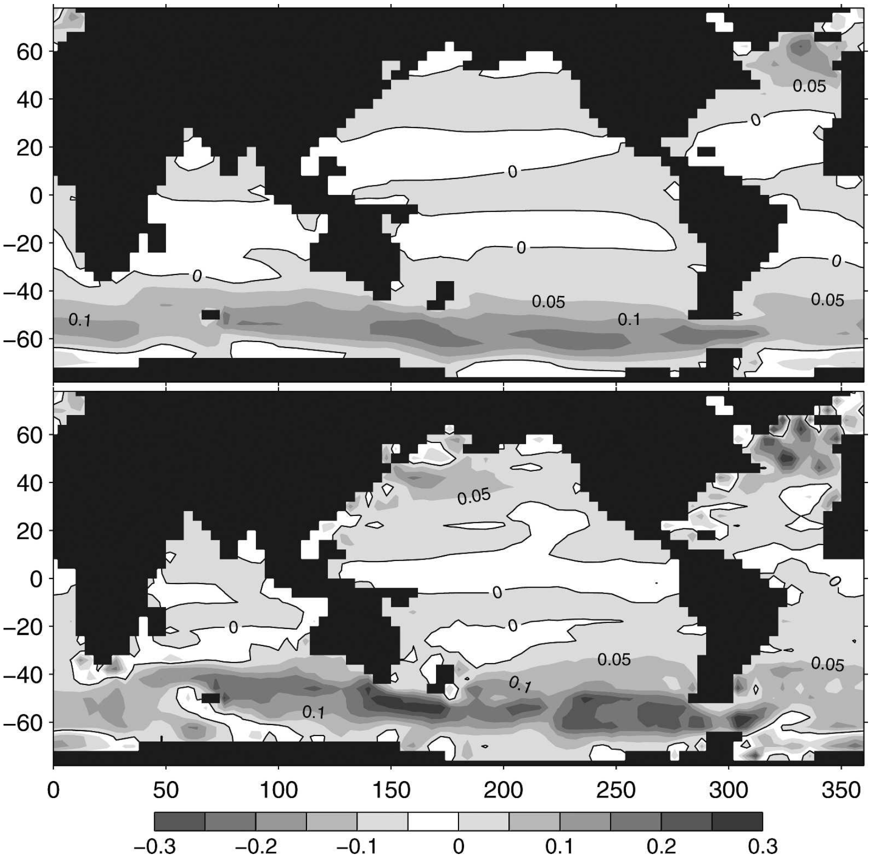

FIG. 4. Same as in Fig. 3, but at 360-m depth.

timized eddy stress shows some hint of a sign reversal relative to that of the initial stress, but this feature is less striking than higher up in the water column.

As illustrated in Fig. 6, the changes in the meridional eddy stress (here at 220 m) are more moderate. As for the zonal component, the first-guess signal is largest along the path of the ACC. However, it is no longer zonally symmetric, but composed of alternate signs up to ±0.15 N m^{-2}. After optimization, the eddy stress is almost unaltered in the open ocean, but significant changes are seen near intense boundary currents. At the depth shown, dipoles of about ±0.15 N m^{-2} have appeared off the eastern South American coast and around the tip of Africa. Such meridional stresses, reflecting zonal eddy buoyancy fluxes, are expected where intense boundary currents have a meridional orientation. However, one must be cautious in interpreting these results since our 4° resolution model does not adequately resolve boundary currents.

The adjusted climatological mean wind stress obtained from calculation E2 is shown in Fig. 7. The adjustments have rather small spatial scales and are largest in the Southern Ocean, the region that is most poorly observed. Significant changes are observed in the northern North Atlantic. This may reflect the poor job done by the model here resulting from the absence of an Arctic basin and, perhaps, the use of a rather simple convection parameterization. Note that adjustments to the meridional wind stress show similar characteristics.

It is tempting to compare the patterns of wind stress adjustments with those obtained by the ECCO project (Stammer et al. 2002), which make use of a much more comprehensive observational set (daily forcings) and many more control parameters in a 2° resolution model. Their adjustment to the mean zonal wind stress bears some resemblance to ours, with relatively small corrections in the Tropics and large ones in the Southern Ocean. However, an interesting feature of the ECCO solution is a strong negative zonal wind stress adjustment around 40°N at the western boundary in the Pacific and Atlantic Oceans. Stammer et al. (2002) attribute this to the difficulty of their 2° model to simulate the intense western boundary current. In our solution, there is a hint of this negative anomaly, but there is also a strong positive eddy stress at 50 m. Thus, it seems that

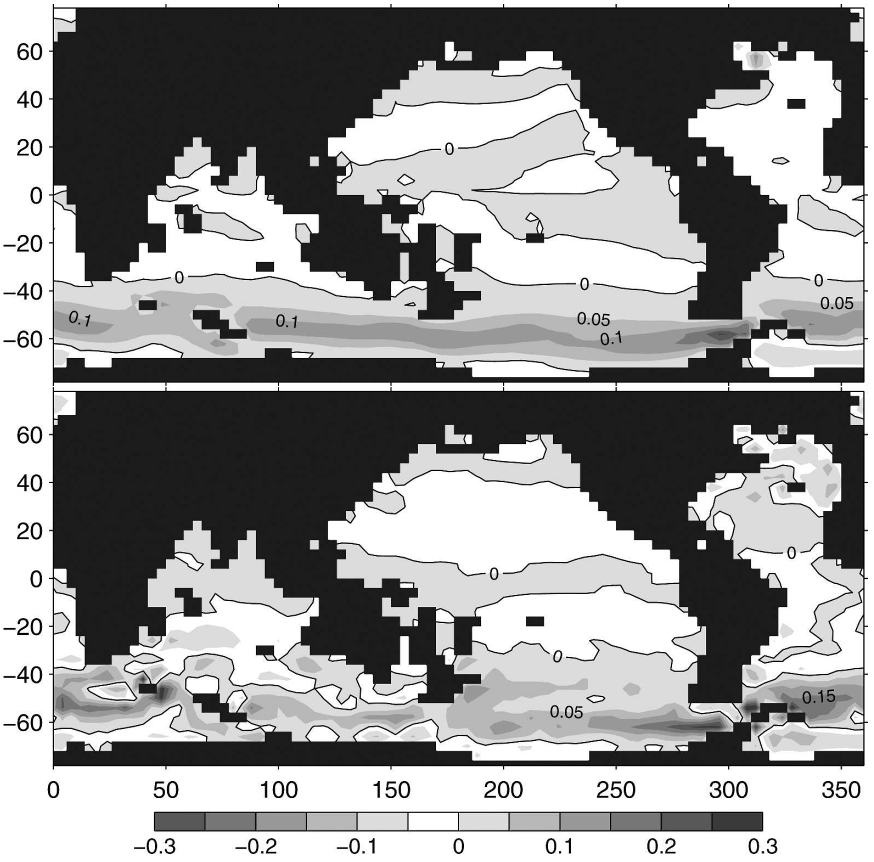

FIG. 5. Same as in Fig. 3, but at 1810-m depth.

the optimized eddy stress has the "physics right" by actually capturing the subscale dynamics that was perhaps erroneously projected onto the wind in the ECCO solutions.

5. Momentum balance and overturning circulation

a. Zonal momentum balance

The results of the optimization can be interpreted in terms of momentum balance. As seen in section 2c, a positive eddy stress can be interpreted as a downward flux of (eastward) momentum. Figure 8 shows the zonally averaged zonal wind stress and zonal eddy stress for the unoptimized (first iteration) and optimized solution (last iteration). The major changes observed in the horizontal maps of the eddy stress are evident: 1) in the ACC, the broadening and equatorward shift of the maximum eddy stress, increasing above 1000 m, smaller below; 2) an intensification near the surface at 40°N; and 3) a sign reversal throughout the Tropics.

At the surface, it is striking how the spatial pattern of optimized eddy stress tends to mirror that of the wind stress. The optimization drives the model toward a momentum balance in which the input of momentum at the surface due to the wind is carried downward by eddy stress. In the Southern Ocean (poleward of 30°S), the magnitude of the initial surface eddy stress is typically 10%–20% of the wind stress, whilst it ranges between 25% and 100% after optimization. The same order of magnitudes apply to the northern latitudes poleward of 30°N. In the Tropics, the sign of the eddy stress tends to "follow" the winds, changing sign in the trade wind belt—this is clearly seen in the horizontal maps plotted in Figs. 3 and 4.

A simplified steady-state zonal momentum equation can be written, using Eq. (13), as

$$fv_{\mathrm{res}} - \frac{1}{\rho_o}\partial_x p + \frac{1}{\rho_o}\partial_z \tau_x^w + \frac{1}{\rho_o}\partial_z \tau_x^e = R, \qquad (17)$$

which describes the balance between the Coriolis force, the pressure gradient, the wind stress divergence, and the eddy stress divergence, summing to form a residual

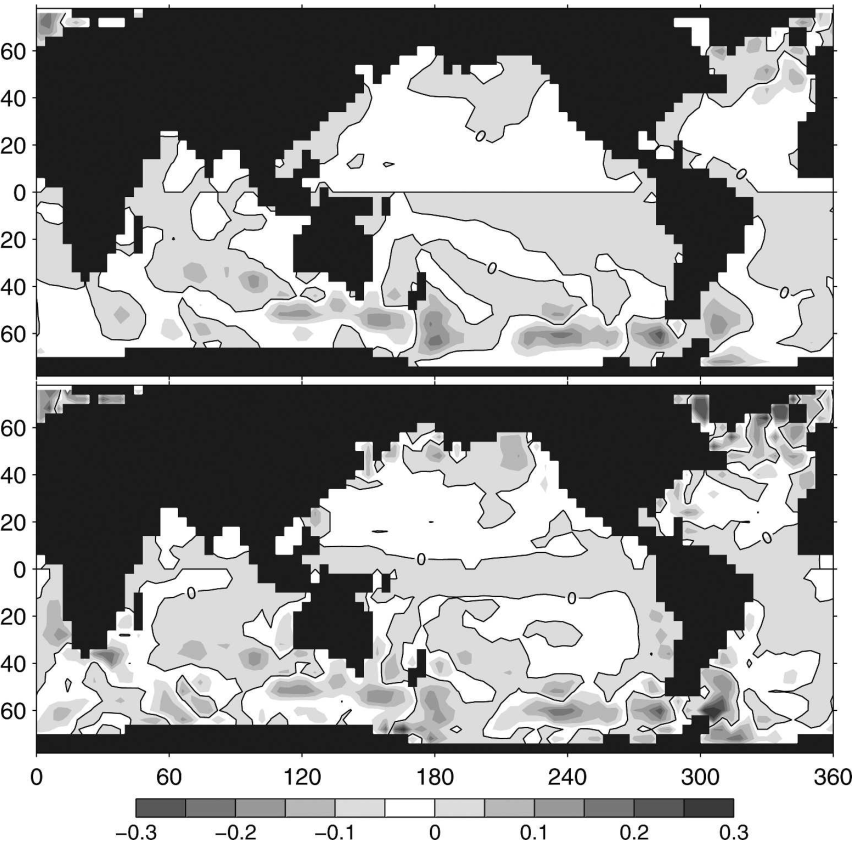

FIG. 6. Same as in Fig. 3, but for the meridional eddy stress at 220-m depth.

R comprising advection, tendency, and frictional terms. In the balances shown below, R (by far dominated by horizontal viscosity) makes only a small contribution.

By vertically integrating Eq. (17)—from the bottom $z = -D(x)$ to the sea surface $z = 0$—and zonally along a latitudinal circle C, the Coriolis force (by continuity) and the eddy stress divergence (by dint of boundary conditions) sum to zero to yield

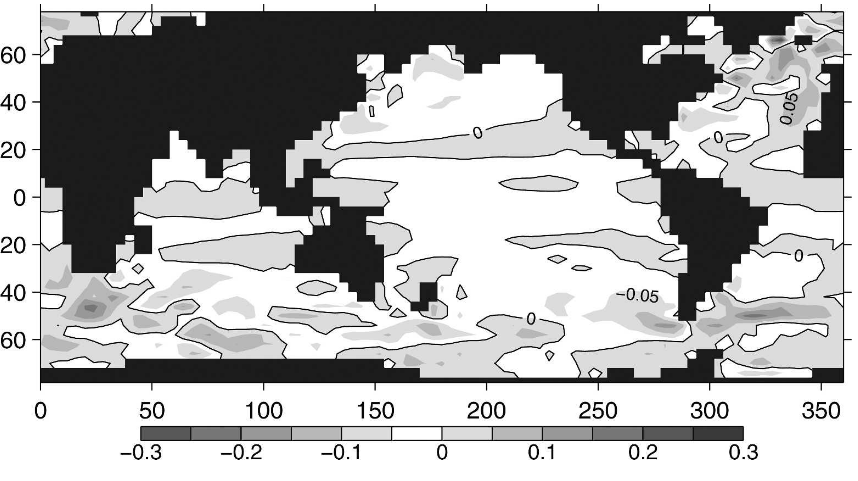

FIG. 7. Adjustment to the observed annual mean zonal wind stress from E2. The contour interval is 0.05 N m^{-2}, and the zero contour is highlighted.

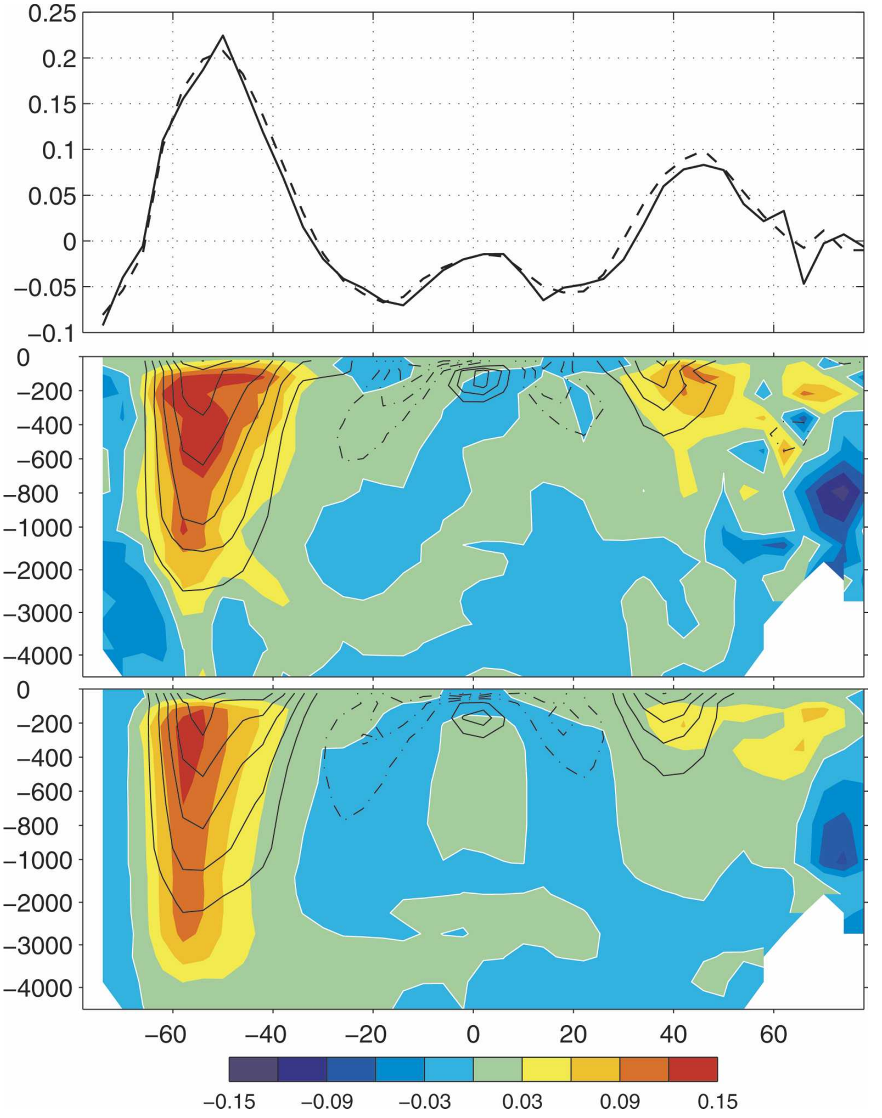

FIG. 8. (top) Zonal mean observed (dashed–dotted) and adjusted (solid) zonal wind stress (N m^{-2}). Zonal mean zonal eddy stress (N m^{-2}; colors) and zonal velocity (m s^{-1}; contours) (middle) before (first guess) and (bottom) after (last iteration of E2) optimization. The eddy stress contour interval is 0.03 N m^{-2}, and the zero contour is highlighted. The contour interval of the velocity is 0.01 m s^{-1}; positive and negative values are solid and dashed lines, respectively.

$$\oint_C \tau_x^w(0)\,dx - \oint_C \frac{p(-D)}{\rho_o}\frac{\partial D}{\partial x}\,dx = \oint_C \int_{-D}^{0} R\,dx\,dz. \tag{18}$$

The integral balance is then a simple one in which the momentum input by the wind at the surface is ultimately balanced by topographic form stress due to pressure gradients across continents and/or seamounts. Because of the smallness of frictional terms, this integral balance is indeed well satisfied at each iteration. However, it provides no information about the process by which momentum is transferred downward in the water column. As we shall see, eddy stresses play a significant role in this vertical transfer.

Figure 9 shows the terms in Eq. (17) when zonally and then vertically integrated over the top layer (0–50 m; top) and a middepth layer (2250–2740 m; bottom) and time averaged over the first iteration of E1. Before optimization, the wind stress at the surface is almost entirely balanced by the Coriolis force. Following Straub (1993), who analyzed the ACC balance in terms

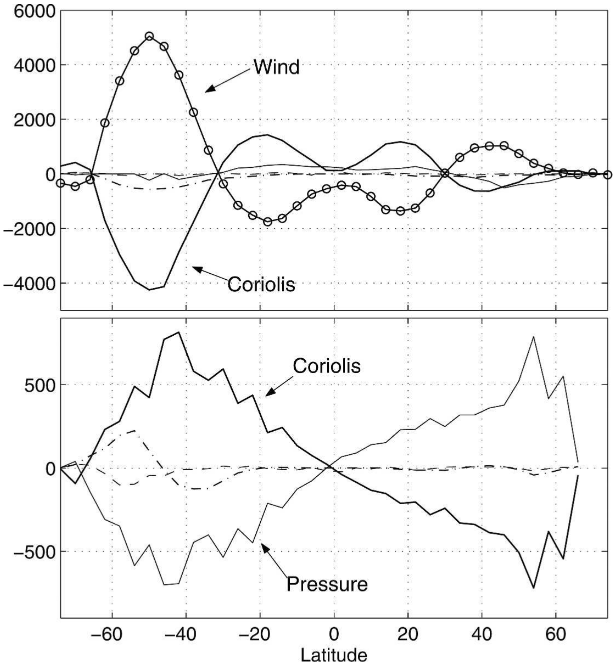

FIG. 9. Zonally integrated zonal momentum balance vertically integrated over (top) the first layer (0–50 m) and (bottom) a middepth layer (2250–2740 m) for the first iteration. Plotted are the wind stress force (circle), the Coriolis force on the residual flow (thick solid), the pressure gradient force (thin solid), the eddy stress divergence (dashed–dotted), and a residual (dashed) dominated by viscosity terms and particularly the horizontal component. Units: $m^3 s^{-2}$.

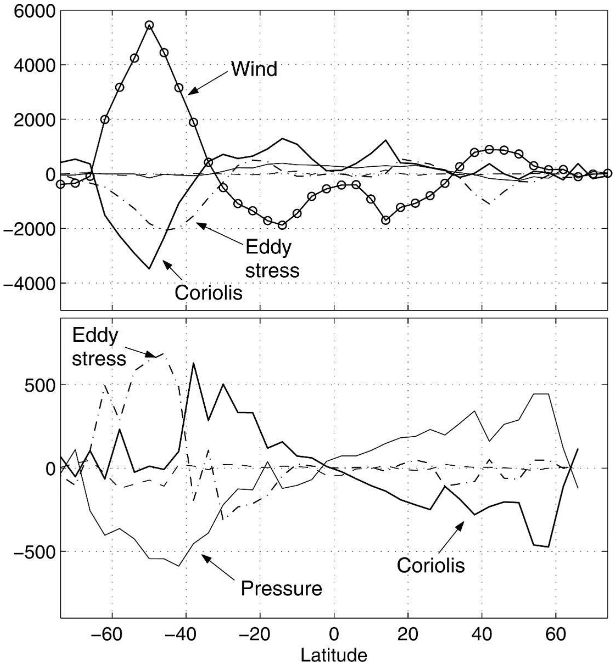

FIG. 10. Same as in Fig. 9, but after optimization (last iteration of E2).

of angular momentum, the positive wind stress torque results in the water parcel moving equatorward to higher values of planetary angular momentum. The vertical transfer of momentum due to eddy stress is negligible in this first iteration, and the residual flow at the surface is approximately the Ekman flow.

After optimization (last iteration of E2; Fig. 10), the eddy stress and Coriolis force contribute in roughly equal measures to balance the wind input in the Southern Ocean (south of 30°S), while in the northern extratropics (north of 30°N), the eddy stress is the main contributor. In the Tropics, the Coriolis force remains the dominant term, although the eddy component is slightly enhanced and is of secondary importance along with the pressure gradient. As a consequence of the increased vertical transfer of momentum by eddy stress, the Coriolis term is reduced and so now the surface flow significantly differs from its Ekman value. Note, in particular, the weaker surface meridional flow across the ACC.

At depth, the balance before optimization is almost exactly between the Coriolis force and pressure gradient (Fig. 9, bottom). Therefore, the residual flow tends to the geostrophic value. After optimization, the balance is widely modified in the ACC region where the vertical eddy stress divergence now balances the pressure gradients. The southward flow is greatly reduced (and no longer well approximated by geostrophic values). In northern latitudes, the nature of the balance is not modified—however both the pressure gradient and Coriolis force are weaker, thus leading to a diminished southward deep flow.

In broad terms then, the optimized solution in the ACC modifies the momentum balance by increasing the local vertical flux due to eddies at the expense of the Coriolis torque. As a result, both the meridional velocity at the surface and at depth is significantly weakened.

b. *Overturning streamfunction*

The modifications to the zonal momentum balance discussed above are reflected in the change in the residual overturning streamfunction of the first and last iterations (Fig. 11). Before optimization, the main cell [+18 Sv (1 Sv ≡ 10^6 $m^3 s^{-1}$)] in the Northern Hemisphere extends southward across the equator and connects to the overturning cell of the Southern Ocean. The latter, driven by westerly winds, flows northward at the surface, downwelling around 40°S. It peaks at 38 Sv near the surface but is relatively weak at depth, never exceeding 20 Sv. Two shallow cells are also evident

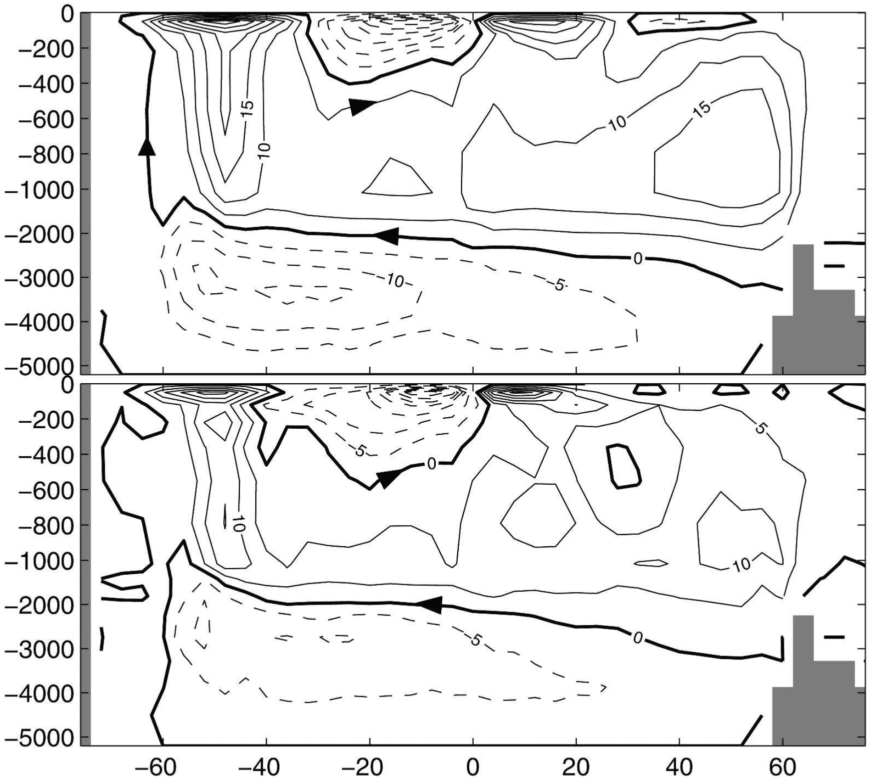

FIG. 11. Overturning streamfunction averaged over the 100 yr of (top) the first iteration of E1 and (bottom) the last iteration of E2. The positive and negative contours are solid and dashed, respectively. The zero contour is highlighted, and the contour interval is 5 Sv.

straddling the equator. They are associated with poleward Ekman transport driven by the trade winds. Last, there is an abyssal cell of strength ~16 Sv between 60°S and 60°N. It flows southward around 2500 m, sinks, and returns at depths below 3500 m. The Antarctic cell associated with the formation of Antarctic Bottom Water is missing in our experiment probably because of poorly observed and represented forcings and the absence of a sea ice component in our model.

The relatively weak Southern Ocean overturning cell obtained here is expected from the TEM framework. The eastward wind stress in the Southern Hemisphere drives strong equatorward Eulerian circulation at the surface, sinking in the subtropics and poleward return flow at depth. This mechanically driven flow tends to tilt up the isopycnal surfaces of the Southern Ocean, thus creating available potential energy. Opposing this tendency is the circulation associated with eddies, which drives flow toward the pole at the surface and equatorward at depth—the zonal integral of $\tau_x^e/(\rho_o f)$ can be interpreted as a streamfunction for the meridional eddy-induced circulation whose pattern is similar to the zonally averaged τ_x^e shown in Fig. 8. Consistent with the eddy-induced circulation being associated with baroclinic instability, it tends to remove available potential energy by flattening isopycnal surfaces. The two effects, which together form the residual circulation, partially cancel one another, resulting in the relatively weak Deacon cell observed in Fig. 11 (top) and found in the studies of Danabasoglu and McWilliams (1995) and Hirst and McDougall (1998). The optimized solution is one in which the residual overturning circulation becomes even weaker (but with broadly similar pattern). In the Northern Hemisphere the overturning cell is also reduced (from 18 to 12 Sv) but remains connected to the overturning circulation of the Southern Ocean. Last, the deep abyssal cell is reduced from 16 to 10 Sv.

c. *Discussion of the ACC*

These findings are consistent with idealized numerical and theoretical studies of the ACC. Marshall (1981) discussed the role of eddies in transferring momentum down in the water column in a zonal-average model with parameterized eddies, motivated by numerical work described in McWilliams et al. (1978). Using quasigeostrophic models with topography, Treguier and McWilliams (1990), Wolff et al. (1991), and Marshall et al. (1993) described how the wind stress is transferred downward by the eddy stress to the bottom where it is balanced by topographic form stress. Admittedly, these studies have serious limitations in the treatment of topography and the absence of buoyancy forcing. Indeed the early study of Johnson and Bryden (1989) developed a simple theoretical model of the ACC in which they assumed that the wind stress is entirely transferred downward by the eddy stress. These studies should be contrasted with Warren et al. (1996), who, setting the eddy contribution to zero, argue that the wind stress is entirely balanced by the Coriolis force associated with northward Ekman transport, which is then the transport acting on tracers at the surface. This picture is indeed very similar to the one obtained at the first iteration in which the eddy stress is relatively weak (Fig. 9). The extreme views of Warren et al. (no eddies) and Johnson and Bryden (eddies exactly balance the wind) lead to two very different dynamical scenarios:

- In Warren et al. (1996), the eddy-induced circulation is zero, and the residual circulation is entirely Eulerian and large in magnitude with strong flow at the surface balanced by a deep southward geostrophic flow supported by pressure gradients across the topography. The circulation is closed by a large cross-isopycnal flow in the interior—see the Eulerian streamfunction in the Fine-Resolution Antarctic Model (FRAM) model for an example (Doos and Webb 1994).
- In Johnson and Bryden (1989), the eddy stress exactly balances the wind stress and transfers it down the water column to the bottom. The eddy-induced circulation exactly opposes the Eulerian circulation, and the residual circulation is zero (see Karsten et al. 2002 for a numerical illustration).

Marshall and Radko (2003) present analytical models of the ACC in which there is a three-way balance between Coriolis torque (on the residual flow), eddy stresses, and wind stress, much like that observed in the optimized solution presented here. Our optimized solution suggests that the eddy contribution to the transport is indeed essential if we are to reproduce the observed distribution of temperature; that is, the residual circulation needs to be much weaker than the Eulerian one, demanding a significant eddy-induced component and thus an eddy stress to sustain it. Moreover, we find that eddy stresses also make a major contribution in the Northern Hemisphere coinciding with the latitude of eastward flowing jets—the Kuroshio and the Gulf Stream—around 40°N.

6. Implication for eddy parameterization in models

a. *Eddy diffusivities*

As a straightforward application, we deduce 3D maps of horizontal eddy diffusivities from the optimized eddy stress. We have already noted the equivalence, in the planetary geostrophic limit, between the GM parameterization and the TEM framework with an eddy stress formulated as in Eq. (16). The latter, derived assuming that eddy buoyancy fluxes are directed down the mean buoyancy gradient, was used with a uniform eddy diffusivity κ to compute the first-guess eddy stress. Inverting the formula provides an estimate of the "optimal" κ as a function of space, namely,

$$\kappa = \frac{(\mathbf{\Psi}^* \times \mathbf{s}_\rho) \cdot \hat{\mathbf{z}}}{|\mathbf{s}_\rho|^2}. \tag{19}$$

The optimal κ is estimated from the last iteration of E2 (results from E1 are very similar and therefore not shown). In practice, to avoid dividing by vanishingly small slopes (less than 10^{-4}), only the maximum of $|\mathbf{s}_\rho|^2$ and 10^{-8} is used in the computation. Figure 12 displays the zonal mean (top) and the vertical mean over the upper ocean (0–1200 m; bottom) of the inferred diffusivity. Before spatial averaging, values exceeding 10^4 $\mathrm{m^2\,s^{-1}}$ (making up less than 0.7% of ocean points but which we consider to be spurious) were removed.

Although the inferred κ is somewhat noisy, it has a well-defined horizontal and vertical large-scale pattern. It is positive in the Southern Ocean (south of 30°S) and the Northern Hemisphere midlatitudes (between 30° and 50°N), and negative in the Tropics between 20°S and 20°N. The amplitude reaches $\pm 4000\ \mathrm{m^2\,s^{-1}}$ in the western boundary currents although the largest values may be due to gridpoint noise. The same horizontal pattern is observed throughout the water column. However it is surface intensified with much smaller amplitude at depth (Fig. 12, top). Peak values are found in near-surface layers, about 100 m deep in the midlatitudes for the positive values and 400 m deep in the Tropics for the negative values.

The gross characteristics of the optimal κ reflect the changes in the eddy stress. And indeed, the results are very robust to the computational details. Only the amplitude of κ in the Tropics where eddy stresses and isopycnal slopes are the smallest is sensitive to the choice of the minimum squared slope (10^{-8} here) although it always remains negative. The unoptimized solution leads, by the same computation, to a fairly

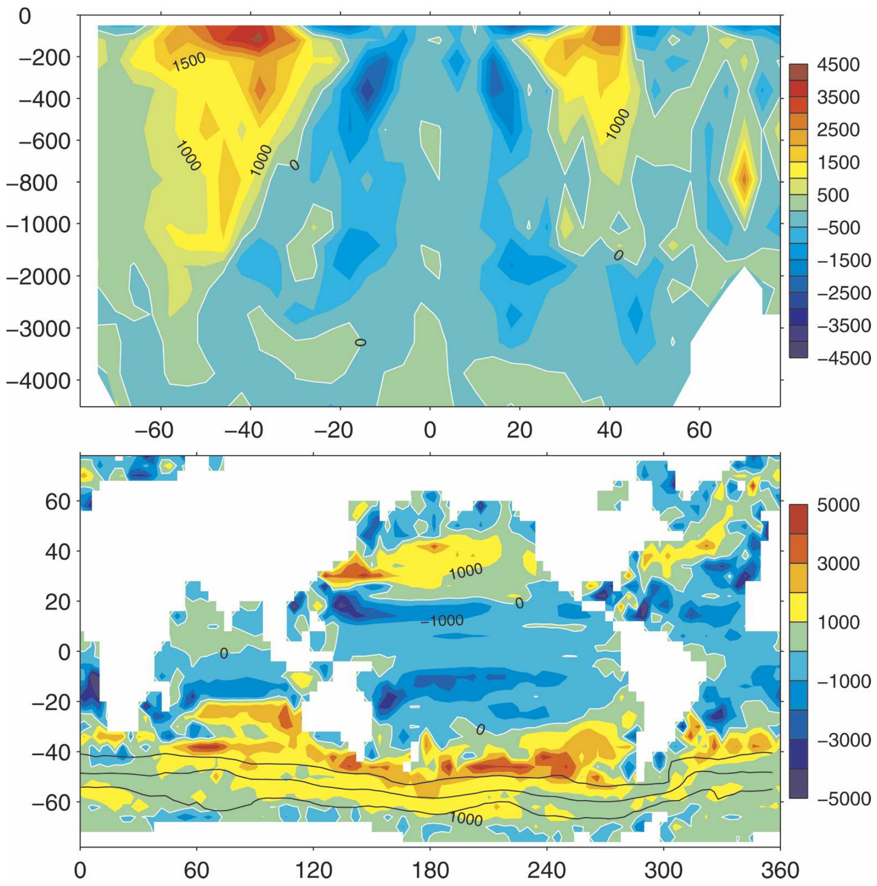

FIG. 12. Inferred horizontal eddy diffusivity κ ($m^2\,s^{-1}$): (top) zonal mean and (bottom) vertical mean over the thermocline (0–1200 m). The contour intervals are (top) 500 and (bottom) 1000 $m^2\,s^{-1}$. The thick line indicates the zero contour. Also indicated in the bottom panel are the 10-, 70-, and 130-Sv contours of the barotropic streamfunction.

uniform value of about 1000 $m^2\,s^{-1}$ because it is close to a GM calculation with a prescribed constant diffusivity. Thus, during the optimization, the inferred κ moves away from uniformity to take on a rather complex structure with values substantially higher (near the surface) and lower (at depth) than the 1000 $m^2\,s^{-1}$ commonly used in a coarse-resolution model.

A number of features of the inferred κ in middle latitudes are rather satisfying. For example, the largest amplitudes are broadly collocated with intense currents and thus intense eddy activity—note the westward intensification of κ in the middle latitudes of the Pacific and southern Atlantic and the relatively strong patch of positive κ along the path of the Gulf Stream. Diffusivities derived from Lagrangian drifters show such westward intensification but are much larger than ours (about $10^4\,m^2\,s^{-1}$ in the Kuroshio; e.g., Zhurbas and Oh 2003). However, note that such estimates are affected by mean flow and shear dispersion and do not necessarily reflect the diffusivities across the mean tracer contours, which is the focus here. A very interesting feature is the presence of large diffusivities on the *equatorward flank* of the ACC (Fig. 12, bottom). This is also captured in the "effective diffusivity" calculations of Marshall et al. (2005, manuscript submitted to *J. Phys. Oceanogr.,* hereinafter MSJH), in which tracer advection driven by satellite altimetry is used to infer surface horizontal diffusivities in the Southern Ocean. MSJH argue that large-scale PV gradients, which are strong at the axis of the ACC, inhibit the lateral dispersal of fluid parcels there, leading to smaller values of κ. On the equatorial flank, however, where PV gradients are much weaker, there is no such inhibition, and the diffusivities reach a maximum. This is reminiscent of the pattern of eddy diffusivities observed in the atmosphere: effective diffusivities peak on the equatorial flank (tropospheric side) of the middle-latitude jet stream (see Haynes and Shuckburgh 2000).

The negative diffusivity obtained in the Tropics, however, is a puzzling result. Indeed, the modeling work of McWilliams and Danabasoglu (2002) combined with observations (Roemmich and Gilson 2001) suggests large positive values of about 2000 $\mathrm{m^2\,s^{-1}}$ in the Tropics. The coarse horizontal and vertical resolution of our model is expected to be especially damaging to the dynamics as the equator is approached. In particular, the erroneous horizontal mixing of momentum appears to bias the optimization because the eddy stress tends to compensate for momentum mixing in the Tropics (not shown). The distortion is significant as these two terms, albeit relatively small, are of the same order of magnitude. This effect is probably not seen in the ACC or the western boundary currents because the eddy stress is much larger than the horizontal mixing of momentum there (at least in our model). Note also that the small Rossby number approximation used to derive the residual-mean momentum Eq. (13) is another cause of concern near the equator. It is therefore tempting to dismiss these negative κs as an artifact of the combination of a distorted dynamics and small eddy stresses in the Tropics.

In Fig. 13, the vertical variation of κ averaged over the area where it is positive is plotted along with the vertical variation in N^2 normalized by its surface value N^2_{ref}. We see that, over the main thermocline, the two vary together, suggesting that

$$\kappa = \frac{N^2}{N^2_{\mathrm{ref}}}\kappa_{\mathrm{ref}}, \tag{20}$$

where κ_{ref} is the diffusivity at the reference level. Equation (20) is the translation in terms of diffusivity of the modified dynamical balance achieved through the optimization. Substituting Eq. (20) into Eq. (16), we obtain

$$\begin{aligned}\tau^e &= \rho_o f\kappa(s_{\rho y}, -s_{\rho x}) = \rho_o f\kappa\frac{(-\overline{b}_y, \overline{b}_x)}{N^2}\\ &= \rho_o f\kappa_{\mathrm{ref}}\frac{(-\overline{b}_y, \overline{b}_x)}{N^2_{\mathrm{ref}}},\end{aligned} \tag{21}$$

which emphasizes that the N^2-dependence of κ gives an eddy stress in phase with the surface winds and currents (meridional buoyancy gradient) rather than the isopycnal slopes. This captures the changes of the eddy stress observed during the optimization in the ACC and in the northern midlatitudes (see Fig. 8).

The N^2-dependence of the eddy diffusivity may perhaps be rationalized by invoking a mixing length hypothesis. Following McWilliams and Danabasoglu (2002), κ scales as $V'L_m$, where V' and L_m are the horizontal eddy velocity and mixing length scales. Introducing an eddy turnover time scale $T_e = L_m/V'$ leads to $\kappa \sim L_m^2/T_e$. If the mixing length is set by the eddy scale and is proportional to the Rossby deformation radius [see the discussion in Visbeck et al. (1997) and Stammer (1997)], and the eddy turnover time scale does not vary dramatically with depth, then a κ that depends on N^2 is implied.

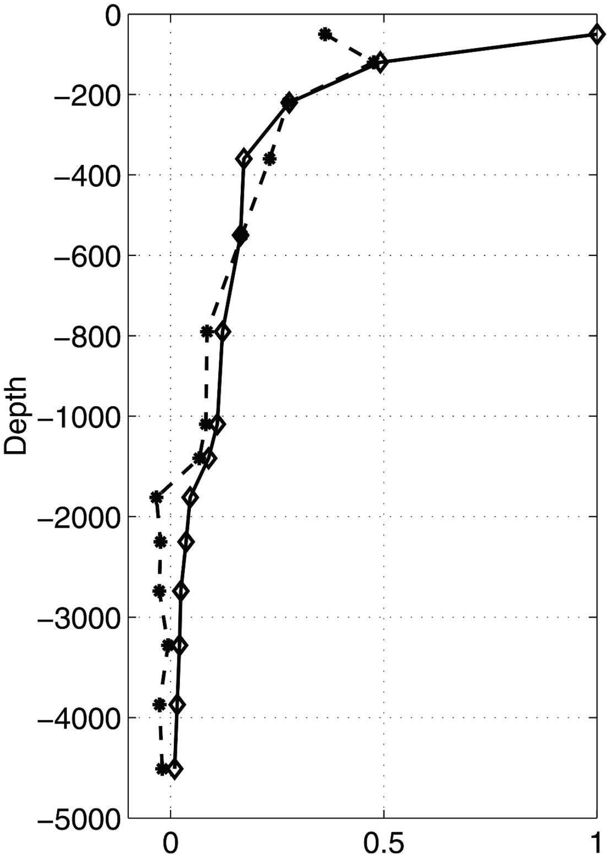

FIG. 13. Averaged vertical profile of the inferred eddy diffusivity κ (divided by 6000 $\mathrm{m^2\,s^{-1}}$; solid) and of the buoyancy frequency N^2 normalized by its surface value (dashed). The averaging area is extended from 65° to 30°S and from 30° to 45°N where the diffusivities are mainly positive.

From another perspective, κ is expected to peak at the steering level of unstable modes where the phase speed of eddies equals the mean flow velocity and eddy–mean flow exchanges are maximized (Green 1970). Gill et al. (1974) conducted a linear stability analysis of various exponential profiles of stratification and velocity. They found that, in the case of baroclinic instability, the steering level was very close to the surface (within the top 500 m), as was the region of maximum extraction of mean potential energy.

The N^2-dependence is appealing because it offers a straightforward extension of the GM eddy parameterization in which the diffusivities are surface intensified. We implement and test this idea in the following section.

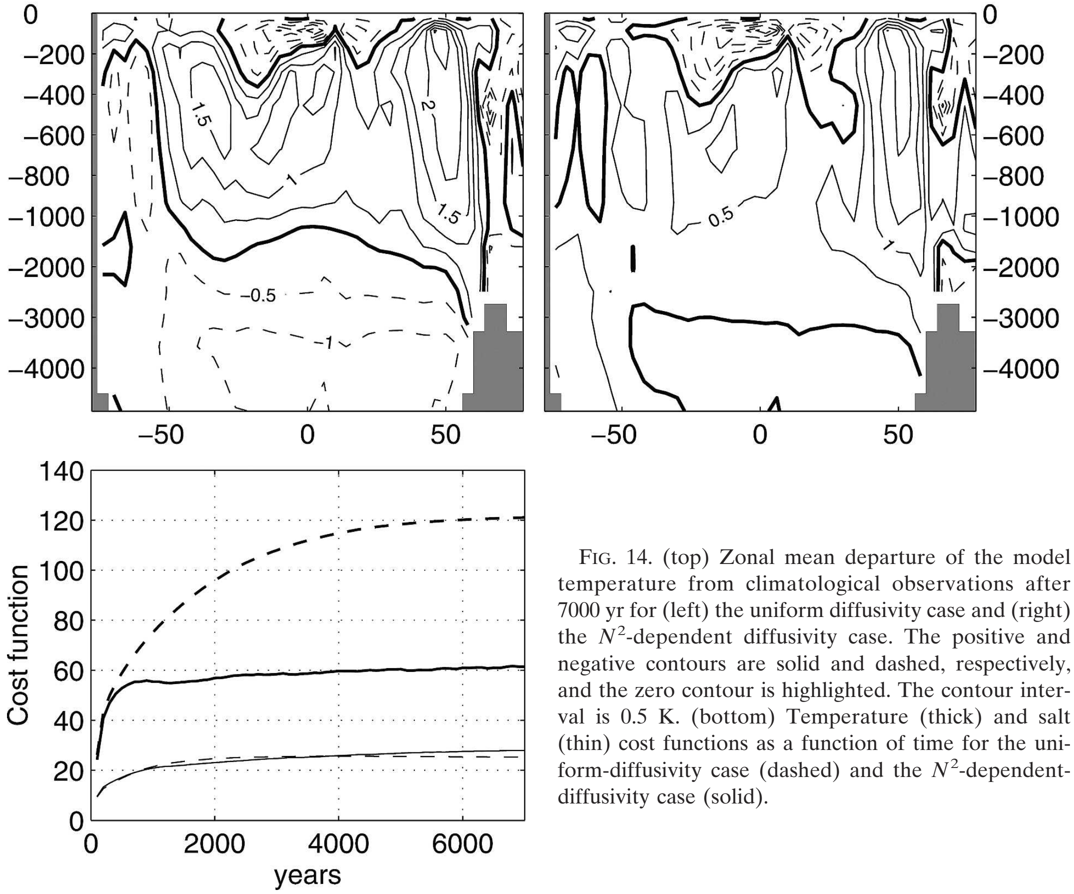

FIG. 14. (top) Zonal mean departure of the model temperature from climatological observations after 7000 yr for (left) the uniform diffusivity case and (right) the N^2-dependent diffusivity case. The positive and negative contours are solid and dashed, respectively, and the zero contour is highlighted. The contour interval is 0.5 K. (bottom) Temperature (thick) and salt (thin) cost functions as a function of time for the uniform-diffusivity case (dashed) and the N^2-dependent-diffusivity case (solid).

b. An N^2-dependent eddy diffusivity

To evaluate the influence of an N^2-dependent diffusivity [Eq. (20)] relative to a uniform value, we conduct a series of experiments using the GM parameterization scheme. The model setup is identical to that used in the optimization except a conventional Eulerian, rather than a residual, formulation is used, that is, a GM scheme is employed in place of an eddy stress. Each experiment is run out for 7000 yr until it approaches equilibrium.

In the N^2-dependent case, Eq. (20) is implemented. To avoid singularities—for example, when N^2_{ref} goes to zero during a convective event—the ratio N^2/N^2_{ref} is tapered to 1. We set $\kappa_{\text{ref}} = 4000\ \text{m}^2\ \text{s}^{-1}$, as suggested by Fig. 12. The evolution of the temperature and salt cost functions (as defined in the optimization; see appendix) for an N^2-dependent and for a uniform diffusivity of $1000\ \text{m}^2\ \text{s}^{-1}$ is shown in Fig. 14. We see that the use of an N^2-dependent diffusivity significantly improves the ocean state by reducing the temperature cost function by a factor 2 relative to the uniform diffusivity, while the salt cost function is hardly affected. Figure 14 (top) shows the zonal and annual mean difference between the model temperature after 7000 yr and the Levitus climatology for the two cases. Anomalously warm thermocline waters found in the uniform diffusivity case are significantly reduced, particularly in the Southern Ocean. The northern high latitudes appear to be relatively insensitive to the choice of κ, possibly because the large slopes encountered there and the use of a tapering scheme may erase the influence of κ. However, the N^2-dependence greatly improves the deep ocean (below 2000 m), reducing the zonal mean error from -1.3 to -0.3 K. However, the Tropics remain unchanged, if not slightly deteriorated.

The overturning streamfunction associated with the meridional bolus transport is dominated in both cases by a cyclonic cell in the Southern Ocean (not shown). In the uniform-κ cases, the overturning has the same spatial form as that of the isopycnal slope, reaching a maximum of 25 Sv at about 300-m depth on the poleward side of the ACC and extending deep into the ocean, as in previous studies (e.g., Hirst and McDougall 1998). For the N^2-dependent case, as expected, the streamfunction is surface intensified with a maximum of 30 Sv in phase with the core of the ACC.

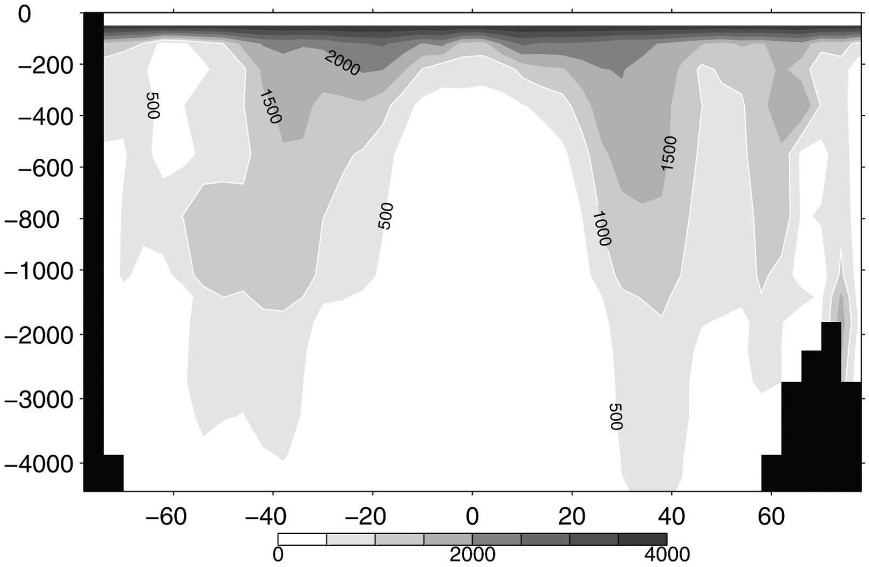

FIG. 15. Zonal mean horizontal eddy diffusivity ($m^2 s^{-1}$) obtained using an N^2-dependence [Eq. (20)] in the GM parameterization scheme. The contour interval is 500 $m^2 s^{-1}$, and the 1000 $m^2 s^{-1}$ contour is highlighted.

Sensitivity of the solution to uniform eddy diffusivity was investigated, and indeed the temperature cost function can almost be reduced by a factor 2 using $\kappa = 2000$ $m^2 s^{-1}$ instead of $\kappa = 1000$ $m^2 s^{-1}$. However, a uniformly large diffusivity has very deleterious effects, reducing the ACC transport at the Drake passage from 107 to 73 Sv, a consequence of the flattening of isopycnal that in turn reduces the current shear and hence the transport. In contrast, use of an N^2-dependent eddy diffusivity yields a Drake passage transport of 129 Sv, more consistent with observations (Rintoul et al. 2001).

In summary, then, an N^2-dependent eddy diffusivity has the virtue of yielding high near-surface values, necessary to capture realistic thermocline properties, and low values at depth allowing strong current shear, as shown in Fig. 15. The vertically averaged diffusivity is typically between 1000 and 500 $m^2 s^{-1}$. Our comparison of the N^2-dependent and uniform diffusivity has not been exhaustive, but it does demonstrate that implementation of a simple N^2-dependent eddy diffusivity in the GM parameterization scheme can lead to substantial improvement of the temperature field and the Drake passage transport of our model.

7. Conclusions

We have described how a residual-mean ocean circulation model and its adjoint can be used to study the regional pattern of subgrid-scale eddy fluxes on a global scale. The effect of the eddies appears as the vertical divergence of an eddy stress whose spatial pattern and magnitude can be adjusted to minimize the drift of the model away from observations.

We find that eddy stresses

1) are large in the ACC, the Kuroshio, and Gulf Stream and
2) have a magnitude comparable to that of the applied wind stress, carrying the momentum imparted by the wind down in the water column.

The implied eddy diffusivities are not spatially uniform but vary in the vertical in the same way as the stratification: they are surface intensified, reaching values as high as several thousand meters squared per second, with much smaller values below. Implementation of a simple N^2-dependent eddy diffusivity in the GM parameterization scheme leads to substantial improvement of the temperature field and the Drake passage transport of a global ocean model.

Acknowledgments. We thank the following colleagues at MIT: Chris Hill and Jean-Michel Campin for help with modeling, Raffaele Ferrari and Alan Plumb for discussions on residual-mean theory, and Carl Wunsch for advice on the least squares method and a careful reading of the manuscript.

APPENDIX

Cost Functions

The departure of the model temperature from observations is measured by a cost function J_1:

$$J_1 = \frac{1}{N}\sum_{i=1}^{N} W_i^{\mathrm{lat}}\left(\frac{\overline{T}_i - \overline{T}_i^{\mathrm{lev}}}{\sigma_i^T}\right)^2, \qquad \text{(A1)}$$

where $\overline{T}_i$ is the 100-yr mean model temperature and $\overline{T}_i^{\mathrm{lev}}$ is the annual mean observed temperature at each grid point i. The differences are weighted by an a priori uncertainty σ_i^T on observations (Levitus and Boyer 1994) and by a latitudinal dependence W_i^{lat}. The error σ_i^T is only a function of depth and varies from 0.5 at the surface to 0.05 K at the bottom of the ocean, mainly reflecting the decreasing temperature variance with depth. Disregarding W_i^{lat} for a moment, a value of J_1 of order 1 means that the model is, on average, within observational uncertainties. Since the complex system of equatorial currents with small vertical and meridional scales cannot be properly resolved by a coarse-resolution model such as the one used here, we choose to down weight points very close to the equator and suppose

$$W_i^{\mathrm{lat}} = \tanh\left(10\frac{\pi}{180}\phi_i\right)^2, \qquad \text{(A2)}$$

where ϕ_i is the latitude. The weights are null at the equator but rapidly increase to 0.5 at ±5° and 0.9 at ±10° to reach values higher than 0.98 poleward of ±15°.

To control the magnitude of the eddy stresses, a second component J_2 is defined by

$$J_2 = \lambda\left[\sum_{\tau_x^{e2}>0.4}(\tau_x^{e2} - 0.4^2) + \sum_{\tau_y^{e2}>0.4}(\tau_y^{e2} - 0.4^2)\right]. \qquad \text{(A3)}$$

The eddy stress can vary unconstrained between −0.4 and 0.4 N m^{-2}; however, a penalty is added beyond those limits. The total cost function of E1 is then $J = J_1 + J_2$, and the scaling factor λ is chosen so that the contribution of J_2 is one order of magnitude smaller than J_1.

In E2, the wind stress is a control variable and the cost function comprises a third component ($J = J_1 + J_2 + J_3$) given by

$$J_3 = \frac{1}{N}\sum_i\left(\frac{\tau_x^w - \tau_{xo}^w}{\sigma_i^x}\right)^2 + \frac{1}{N}\sum_i\left(\frac{\tau_y^w - \tau_{yo}^w}{\sigma_i^y}\right)^2, \qquad \text{(A4)}$$

where τ_{xo}^w and τ_{yo}^w are the observed wind stress (Trenberth et al. 1990) and σ_i^x and σ_i^y are the a priori errors.

REFERENCES

Adcroft, A., C. Hill, and J. Marshall, 1997: Representation of topography by shaved cells in a height coordinate ocean model. *Mon. Wea. Rev.,* **125,** 2293–2315.

Andrews, D. G., and M. E. McIntyre, 1976: Planetary waves in horizontal and vertical shear: The generalized Eliassen-Palm relation and the mean zonal acceleration. *J. Atmos. Sci.,* **33,** 2031–2048.

——, J. R. Holton, and C. B. Leovy, 1987: *Middle Atmosphere Dynamics.* Academic Press, 489 pp.

Canuto, V. M., and M. S. Dubovikov, 2005: Dynamical model of mesoscales in *z*-coordinates. *Ocean Modell.,* **11,** doi:10.1016/j.ocemod.2004.12.002.

Danabasoglu, G., and J. McWilliams, 1995: Sensitivity of the global ocean circulation to parameterizations of mesoscale tracer transports. *J. Climate,* **8,** 2967–2987.

Doos, K., and D. Webb, 1994: The Deacon cell and other meridional cells of the Southern Ocean. *J. Phys. Oceanogr.,* **24,** 429–442.

Ferrari, R., and R. A. Plumb, 2003: The residual circulation in the ocean. *Near-Boundary Processes and Their Parameterization: Proc. 'Aha Huliko'a Hawaiian Winter Workshop,* Honolulu, HI, University of Hawaii at Manoa, 219–228.

Gent, P. R., and J. C. McWilliams, 1990: Isopycnic mixing in ocean circulation models. *J. Phys. Oceanogr.,* **20,** 150–155.

——, J. Willebrand, T. J. McDougall, and J. C. McWilliams, 1995: Parameterizing eddy-induced tracer transports in ocean circulation models. *J. Phys. Oceanogr.,* **25,** 463–474.

Giering, R., and T. Kaminski, 1998: Recipes for adjoint code construction. *ACM Trans. Math. Software,* **24,** 437–474.

Gilbert, J. C., and C. Lemaréchal, 1989: Some numerical experiments with variable-storage quasi-Newton algorithms. *Math. Programm.,* **45,** 407–435.

Gill, A. E., J. S. A. Green, and A. J. Simmons, 1974: Energy partition in the large-scale ocean circulation and the production of mid-ocean eddies. *Deep-Sea Res.,* **21,** 499–528.

Greatbatch, R. J., 1998: Exploring the relationship between eddy-induced transport velocity, vertical momentum transfer, and the isopycnal flux of potential vorticity. *J. Phys. Oceanogr.,* **28,** 422–432.

Green, J. S., 1970: Transfer properties of the large-scale eddies and the general circulation of the atmosphere. *Quart. J. Roy. Meteor. Soc.,* **96,** 157–185.

Haynes, P. H., and E. Shuckburgh, 2000: Effective diffusivity as a diagnostic of atmospheric transport. 1. Stratosphere. *J. Geophys. Res.,* **105,** 22 777–22 794.

Held, I., and T. Schneider, 1999: The surface branch of the zonally averaged mass transport circulation in the troposphere. *J. Atmos. Sci.,* **56,** 1688–1697.

Hirst, A. C., and T. J. McDougall, 1998: Meridional overturning and dianeutral transport in a *z*-coordinate ocean model including eddy-induced advection. *J. Phys. Oceanogr.,* **28,** 1205–1223.

Johnson, G. C., and H. L. Bryden, 1989: On the size of the Antarctic Circumpolar Current. *Deep-Sea Res.,* **36,** 39–53.

Kalnay, E., and Coauthors, 1996: The NCEP/NCAR 40-Year Reanalysis Project. *Bull. Amer. Meteor. Soc.,* **77,** 437–471.

Karsten, R., H. Jones, and J. Marshall, 2002: The role of eddy transfer in setting the stratification and transport of a circumpolar current. *J. Phys. Oceanogr.,* **32,** 39–54.

Kuo, A., R. A. Plumb, and J. Marshall, 2005: Transformed Eulerian-mean theory. Part II: Potential vorticity homogenization and the equilibrium of a wind- and buoyancy-driven zonal flow. *J. Phys. Oceanogr.,* **35,** 175–187.

Levitus, S., and T. P. Boyer, 1994: *Temperatures.* Vol. 4, *World Ocean Atlas 1994*, NOAA Atlas NESDIS 4, 117 pp.

——, R. Burgett, and T. P. Boyer, 1994: *Salinity.* Vol. 3, *World Ocean Atlas 1994,* NOAA Atlas NESDIS 3, 99 pp.

Marotzke, J., R. Giering, Q. K. Zhang, D. Stammer, C. N. Hill, and T. Lee, 1999: Construction of the adjoint MIT ocean general circulation model and application to Atlantic heat transport sensitivity. *J. Geophys. Res.,* **104,** 29 529–29 548.

Marshall, J. C., 1981: On the parameterization of geostrophic eddies in the ocean. *J. Phys. Oceanogr.,* **11,** 1257–1271.

——, and F. Schott, 1999: Open-ocean convection: Observations, theory and models. *Rev. Geophys.,* **37,** 1–64.

——, and T. Radko, 2003: Residual-mean solutions for the Antarctic Circumpolar Current and its associated overturning circulation. *J. Phys. Oceanogr.,* **33,** 2341–2354.

——, D. Olbers, H. Ross, and D. Wolf-Gladrow, 1993: Potential vorticity constraints on the dynamics and hydrography of the Southern Ocean. *J. Phys. Oceanogr.,* **23,** 465–487.

——, A. Adcroft, C. Hill, L. Perelman, and C. Heisey, 1997a: A finite-volume, incompressible Navier Stokes model for studies of the ocean on parallel computers. *J. Geophys. Res.,* **102,** 5753–5766.

——, C. Hill, L. Perelman, and A. Adcroft, 1997b: Hydrostatic, quasi-hydrostatic, and nonhydrostatic ocean modeling. *J. Geophys. Res.,* **102,** 5733–5752.

McWilliams, J., and G. Danabasoglu, 2002: Eulerian and eddy-induced meridional overturning circulations in the Tropics. *J. Phys. Oceanogr.,* **32,** 2054–2071.

——, W. R. Holland, and J. H. S. Chow, 1978: A description of numerical Antarctic Circumpolar Currents. *Dyn. Atmos. Oceans,* **2,** 213–291.

Plumb, R., and R. Ferrari, 2005: Transformed Eulerian-mean theory. Part I: Nonquasigeostrophic theory for eddies on a zonal-mean flow. *J. Phys. Oceanogr.,* **35,** 165–174.

Redi, M. H., 1982: Oceanic isopycnal mixing by coordinate rotation. *J. Phys. Oceanogr.,* **12,** 1154–1158.

Rhines, P. B., 1979: Geostrophic turbulence. *Annu. Rev. Fluid Mech.,* **11,** 404–441.

Rintoul, S., C. Hughes, and D. Olbers, 2001: The Antarctic Circumpolar Current System. *Ocean Circulation and Climate,* G. Siedler, J. Church, and J. Gould, Eds., International Geophysics Series, Vol. 77, Academic Press, 271–302.

Roemmich, D., and J. Gilson, 2001: Eddy transport of heat and thermocline waters in the North Pacific: A key to interannual/decadal climate variability. *J. Phys. Oceanogr.,* **31,** 675–688.

Stammer, D., 1997: Global characteristics of ocean variability estimated from regional TOPEX/Poseidon altimeter measurements. *J. Phys. Oceanogr.,* **27,** 1743–1769.

——, and Coauthors, 2002: Global ocean circulation during 1992–1997, estimated from ocean observations and a general circulation model. *J. Geophys. Res.,* **107,** 3118, doi:10.1029/2001JC000888.

Straub, D. N., 1993: On the transport and angular momentum balance of channel models of the Antarctic Circumpolar Current. *J. Phys. Oceanogr.,* **23,** 776–782.

Treguier, A. M., and J. C. McWilliams, 1990: Topographic influence on wind-driven stratified flow in a β-plane channel: An idealized model for the Antarctic Circumpolar Current. *J. Phys. Oceanogr.,* **20,** 321–343.

——, I. M. Held, and V. D. Larichev, 1997: On the parameterization of the quasigeostrophic eddies in primitive equation ocean models. *J. Phys. Oceanogr.,* **27,** 567–580.

Trenberth, K. E., W. G. Large, and J. G. Olson, 1990: The mean annual cycle in global ocean wind stress. *J. Phys. Oceanogr.,* **20,** 1742–1760.

Visbeck, M., J. Marshall, T. Haine, and M. Spall, 1997: On the specification of eddy transfer coefficients in coarse-resolution ocean circulation models. *J. Phys. Oceanogr.,* **27,** 381–402.

Wardle, R., and J. Marshall, 2000: Representation of eddies in primitive equation models by a PV flux. *J. Phys. Oceanogr.,* **30,** 2481–2503.

Warren, B. A., J. H. LaCasce, and P. E. Robbins, 1996: On the obscurantist physics of "form drag" in theorizing about the Circumpolar Current. *J. Phys. Oceanogr.,* **26,** 2297–2301.

Wolff, J.-O., E. Maier-Reimer, and D. Olbers, 1991: Wind-driven flow over topography in a zonal β-plane channel: A quasi-geostrophic model of the Antarctic Circumpolar Current. *J. Phys. Oceanogr.,* **21,** 236–264.

Zhurbas, V., and I. S. Oh, 2003: Lateral diffusivity and Lagrangian scales in the Pacific Ocean as derived from drifter data. *J. Geophys. Res.,* **108,** 3141, doi:10.1029/2002JC001596.